

Document downloaded from:

<http://hdl.handle.net/10251/65585>

This paper must be cited as:

Sánchez Tovar, R.; Fernández Domene, RM.; Blasco-Tamarit, E.; Garcia-Anton, J. (2015). Synergistic effect between hydrodynamic conditions during Ti anodization and acidic treatment on the photoelectric properties of TiO₂ nanotubes. *Journal of Catalysis*. 330:434-441. <http://hdl.handle.net/10251/65585>.



The final publication is available at

<http://dx.doi.org/10.1016/j.jcat.2015.08.002>

Copyright Elsevier

Additional Information

**SYNERGISTIC EFFECT BETWEEN HYDRODYNAMIC CONDITIONS
DURING Ti ANODIZATION AND H⁺-DOPING ON THE PHOTOCATALYTIC
PERFORMANCE OF TiO₂ NANOTUBES**

**Sánchez-Tovar, R.; Fernández-Domene, R.M.; Martínez-Sánchez, A.; Blasco-
Tamarit, E.; García-Antón, J. ***

*Ingeniería Electroquímica y Corrosión (IEC). Departamento de Ingeniería Química y
Nuclear. ETSI Industriales. Universitat Politècnica de València. Camino de Vera s/n,
46022 Valencia, Spain.*

Tel. 34-96-387 76 32, Fax. 34-96-387 76 39, e-mail: jgarciaa@iqn.upv.es

In the present work, the combined influence of controlled hydrodynamic conditions during Ti anodization and the H⁺ intercalation on the photocatalytic performance of mixed anatase/rutile TiO₂ nanotubes has been studied. Anodized samples were analyzed by means of Field Emission Scanning Electronic Microscopy (FE-SEM), Confocal Raman Microscopy, electrochemical measurements (electrochemical impedance spectroscopy and Mott-Schottky analysis) and photoelectrochemical measurements. It has been observed that the use of hydrodynamic conditions increases the surface area of nanotubes, while H⁺-doping enhances their conductivity. Besides, there is a clear synergistic effect between the hydrodynamic conditions and the H⁺-doping, which results in higher photocurrent densities for the H⁺-doped nanotubes formed under hydrodynamic conditions.

Keywords: TiO₂ nanotubes; hydrodynamic conditions; photocatalysis; electrochemical impedance spectroscopy (EIS); Mott-Schottky analysis.

1. INTRODUCTION

Over the past years, self-organized TiO₂ nanotubes (NTs) fabricated by electrochemical anodization have attracted wide and continuously increasing interest [1-13]. Highly ordered TiO₂ NTs offer unique properties leading to higher photo-conversion efficiency, which makes these nanostructures be suitable for numerous technological applications, such as photocatalytic water splitting.

TiO₂ NTs formed in organic electrolytes (e.g. ethylene glycol) containing a small amount of fluoride ions can be longer (from several to hundreds of μm) and generally have higher photoelectrochemical water splitting efficiency than NTs formed in aqueous electrolytes [4, 7, 11, 14-18]. However, TiO₂ NTs grown in ethylene glycol often show a disintegration of their top end due to chemical etching, which have a “nanograss” appearance [6, 9-14, 16, 18-20]. These structural disorders may interrupt the electron transport and enhance charge carriers recombination, as well as prevent light from passing through the NTs [7, 9, 11, 19].

Schmuki and co-workers have developed a simple approach to eliminate this disorder in TiO₂ NTs formed in ethylene glycol by forming a protective initiation layer on polished Ti samples [14] or by forming a thermal rutile layer [6], thus delaying the chemical etching of the tube tops and hence the formation of “nanograss”. Nevertheless, the diameters of the nanopores of this initiation layer are smaller than those of the NTs beneath it [7, 13, 14, 18], so this porous layer covers part of the tubes, which can limit the performance of the NTs in photocatalysis and dye sensitized solar cells [13, 18]. Moreover, during the anodization process, Ti⁴⁺ dissolved and released towards the

electrolyte can precipitate at the entrance of the nanopores/nanotubes in the form of TiO_2 or $\text{Ti}(\text{OH})_4$ [7], thus partially blocking them.

On the other hand, the efficiency of TiO_2 NTs is usually limited not only by its large band gap, but also by the rapid electron-hole recombination due to trap states. In order to increase the efficiency in TiO_2 NTs, the insertion of elements in the TiO_2 lattice (doped TiO_2) is commonly used to increase its donor density or/and its conductivity [21, 22].

In a previous work [12] it was demonstrated that ill-defined nanotube top morphologies such as “nanograss” was prevented by forming TiO_2 NTs in ethylene glycol under controlled hydrodynamic conditions. Moreover, the porous initiation layer was also partially removed during the anodization process at high Reynolds numbers (Re), thus improving significantly the efficiency of these NTs. The aim of the present work is to study the combined influence of controlled hydrodynamic conditions during anodization and the H^+ intercalation on the tube top morphology of anatase/rutile nanostructures and on their photocatalytic performance. The use of TiO_2 with anatase/rutile phases in its crystalline structure could be beneficial in order to reduce the band gap of TiO_2 and, at the same time, maintain a high conductivity [23]. The influence of the H^+ intercalation on the morphology and photoelectrochemical properties of TiO_2 NTs has been barely studied in the literature [24, 25], but no published study on the effect that hydrodynamic conditions together with the H^+ intercalation have on the properties of the resulting nanotube arrays has been found.

2. EXPERIMENTAL

Anodization was carried out using a Teflon coated titanium rod (8 mm in diameter, 99.3 % purity) as working electrode, i.e. 0.5 cm^2 were exposed to the electrolyte. On the other hand, a platinum mesh was used as counter electrode. Prior to anodization, titanium surface was abraded with 220 to 4000 silicon carbide (SiC) papers, degreased by sonication in ethanol for 2 minutes and dried in a N_2 stream. The samples were then mounted in a rotating electrode to perform the anodization under hydrodynamic conditions using a voltage source. Different Reynolds numbers were used: 0, 200, 400 and 600, which correspond to 0, 1728, 3456 and 5185 rpm. Anodization was performed in ethylene glycol, 1M H_2O and 0.05M NH_4F electrolytes at 55 V during 30 minutes. Current density during anodization was measured versus time. After each test, the titanium rod was sliced to characterize the morphology of the obtained nanostructures by using Field Emission Scanning Electron Microscopy (FE-SEM). In order to transform amorphous TiO_2 to a mixed anatase/rutile phase structure, the anodized samples were annealed at $650 \text{ }^\circ\text{C}$ for 1 hour. The crystalline microstructure of TiO_2 was examined by means of a Raman Confocal Laser spectroscopy (“Witec Raman microscope”). For these measurements, a 632 nm neon laser with $420 \text{ } \mu\text{W}$ was used.

In order to add H^+ to the obtained nanostructures (doped-nanostructures), samples were immersed in an 1M HClO_4 solution, applying $-1.5 \text{ V}_{\text{Ag}/\text{AgCl}}$ during 3 seconds [25]. In this way, Ti^{+4} was reduced to Ti^{+3} and, at the same time, H^+ was intercalated into the TiO_2 lattice. In order to perform the H^+ intercalation, a three electrode electrochemical cell was used. The TiO_2 NTs after annealing served as working electrode, while a

saturated Ag/AgCl (3 M KCl) electrode was the reference electrode, and a platinum tip was the counter electrode.

For the electrochemical and photoelectrochemical water splitting tests, an electrochemical cell with the same electrodes and electrode configuration than the used for doping the samples, was employed. The area of the TiO₂ nanostructures (working electrode) exposed to the test solution was 0.13 cm². The electrochemical measurements were conducted in a 0.1 M Na₂SO₄ solution using an Autolab PGSTAT302N potentiostat under dark conditions (without irradiation). EIS experiments were conducted at the open circuit potential (OCP) over a frequency range from 100 kHz to 10 mHz with a 10 mV (peak to peak) signal amplitude. Mott–Schottky plots were subsequently obtained by sweeping the potential from the OCP in the negative direction at 10 mV s⁻¹ with an amplitude signal of 10 mV at a frequency value of 10 kHz.

The photoelectrochemical experiments were carried out under simulated sunlight condition AM 1.5 (100 mW cm²) in a 1M KOH solution. Photocurrent vs. voltage characteristics were recorded by scanning the potential from -0.8 V_{Ag/AgCl} to +0.55 V_{Ag/AgCl} with a scan rate of 2 mV s⁻¹. Photocurrent transients as a function of the applied potential were recorded by chopped light irradiation (60 s in the dark and 20 s in the light). Samples were left at +0.55 V_{Ag/AgCl} in the light for one hour, in order to evaluate their stability to the photocorrosion attack.

3. RESULTS AND DISCUSSION

3.1. Field Emission Scanning Electron Microscopy (FE-SEM)

Figure 1 shows the morphology of the nanostructures obtained by electrochemical anodization of TiO₂ under static and hydrodynamic conditions (Figure FE-SEM a and b, respectively). Under the studied flowing conditions (from Re = 200 to Re = 600) the morphology of the TiO₂ is very similar and non remarkable differences should be mentioned, for this reason **Figure 1** shows, for instance, the data corresponding to the TiO₂ nanostructure synthesized at Re = 600. From the FE-SEM images it can be observed that the morphology of the TiO₂ anodized in ethylene glycol based electrolytes presents a porous top layer (initiation layer), i.e., the interpore space is connected. This layer has pores whose diameter is smaller than that of the nanotubes beneath it (see **Figure 1c**) and hence partially blocks the mouth of the underneath larger NTs.

Hydrodynamic conditions mainly affect in the top morphology and in the thickness of the NTs. Regarding the former, flowing conditions increase the diameter of the pores present in the porous initiation layer, from mean values of 70 nm to 99 nm, working at Re = 0 and 600, respectively (**Figures 1a and 1b**). Additionally, as the Re number is increased, the initiation layer becomes increasingly etched and the entrances of the real tube layer become apparent and accessible. On the other hand, regarding the effect of flowing conditions on the thickness of the TiO₂ layers, stirring allowed an accelerated growth of TiO₂ nanotube layers. **Figure 1d** shows the influence of Re on the thicknesses of the NTs. According to this, the use of flowing conditions during electrochemical anodization of TiO₂ seems to be beneficial in order to increase the surface area available for photocatalytic purposes. Despite the fact that the thickness of

the layers formed under hydrodynamic conditions increases in almost 2 μm with respect to the value at $\text{Re} = 0$, the thicknesses of the layers remain constant if the samples anodized under rotation are compared.

Doped TiO_2 FE-SEM images (not shown), reveal that H^+ insertion does not produce significant changes neither in surface morphology nor in the cross section of the NTs, regardless of the Re .

3.2. Raman Confocal Laser Microscopy

Figure 2 shows the spectra of as-prepared and annealed TiO_2 nanostructures for $\text{Re} = 600$.

The Raman spectra can elucidate the crystallinity of the NTs by evaluating the peaks formed from the molecular bonds. The as-prepared TiO_2 NTs (not annealed) are characterized by a broad spectra from 100 to 1000 cm^{-1} due to amorphous titania [26]. On the other hand, **Figure 2** shows that the Raman peaks corresponding to the NTs annealed at 650 $^\circ\text{C}$ present signals of anatase and rutile. In this way, the anatase phase (**A in Figure 2**) shows major Raman bands at roughly 142, 192, 392, 515 and 640 cm^{-1} . All these bands correspond to the five Raman-active modes of anatase phase with the symmetries of E_g , E_g , A_{1g} , B_{1g} and E_g , respectively [23, 27, 28]. **Figure 2** also shows the presence of rutile phase (**R in Figure 2**) with a band at approximately 450 cm^{-1} (E_g mode). On the other hand, the second characteristic peak of rutile, which might appear at roughly 615 cm^{-1} as a shoulder of the anatase signal at 640 cm^{-1} , only appears with a very low intensity and is barely appreciated in any of the annealed samples [29]. This confirms that annealing at 650 $^\circ\text{C}$, rutile phase is in minority in comparison to anatase

one. It is important to point out that interfacial vibrations are present in NTs (due to their nanoscale size and their high surface area) and they may broaden and shift the bands to slightly lower wavelengths [30].

The rest of the formed nanostructures present similar Raman spectra, including the doped samples. This fact indicates that all the TiO₂ NTs possess anatase and rutile in their crystalline structure.

3.3. Current density transients during anodization

Figure 3 shows the current density transients obtained during the potentiostatic anodization of Ti at 55 V at different Re.

In all cases, regardless of the hydrodynamic conditions, current density dropped sharply from a high initial value in the first seconds of anodization (stage I in **Figure 3**) due to the fast formation of an insulating compact oxide layer [4, 10, 16-18]. Subsequently, the nucleation of irregular nanoscale pores due to the dissolution of the initial compact oxide film by the action of fluoride ions resulted in an increase in the anodization current density [4, 10, 18], since this phenomenon led to a decrease in the resistance of the compact layer as the reactive area increased (stage II in **Figure 3**). This increase was much more marked and fast in the case of anodization under hydrodynamic condition, especially at Re = 400 and Re = 600, reaching a maximum after about 400 seconds. In contrast, the anodization current density under stagnant conditions (Re = 0) and at Re = 200 increased at a slower rate, reaching significantly lower values than under hydrodynamic conditions. Afterwards, anodization current density decreased at a small rate in the case of Re = 400 and Re = 600, while at Re = 0 and Re = 200 anodization

current density remained relatively constant until the end of the anodization process (stage III in **Figure 3**). This last stage in the process of anodization represents the formation of a regular nanopore or nanotube layer and the establishment of an equilibrium between field assisted oxide formation and dissolution [10, 18, 31]. The higher current density values obtained under hydrodynamic conditions in the three stages indicate that the different process that took place during anodization were controlled by the diffusion of either fluoride ions inward or the diffusion of the complex species $[\text{TiF}_6]^{2-}$ outward from the tube bottom [32].

3.4. Photocurrent measurements

Representative photovoltammograms for TiO_2 NTs synthesized at different Re and for H^+ -doped TiO_2 NTs at $\text{Re} = 0$ and $\text{Re} = 600$ are shown, respectively, in **Figure 4a** and **Figure 4b**. It can be observed that photocurrent densities increased with increasing Re and that the photoresponse was clearly enhanced in the H^+ -doped TiO_2 NTs, particularly at $\text{Re} = 600$.

The high photocurrent densities obtained for samples anodized under hydrodynamic conditions are directly related to an increase in the active area of the NTs exposed to the electrolyte with increasing Re. As explained above when describing the SEM images, hydrodynamic conditions during anodization resulted in higher NTs lengths and higher diameters of the nanoporous initiation layer, as well as in a partial removal of the nanoporous initiation layer.

According to several authors [25, 33] the polarization of the TiO₂ NTs at cathodic potentials and the H⁺ intercalation into their structure can suppress the recombination losses associated with the capture of electrons by trap states which originate mainly from incompletely coordinated Ti⁴⁺ surface sites (dangling bonds states) [25, 33-38]. Hence, the blocking or passivation of these charge recombination sites could be the cause of the photocurrent enhancement of the H⁺-doped samples upon illumination [25, 33, 34, 38].

On the other hand, Boschloo et al. [39] observed an increase in donor density when intercalating H⁺ cations in a TiO₂ film, caused, according to their explanations, by the role of interstitial hydrogen atoms as donor impurities. This fact could also explain the increase in photocurrent for the H⁺-doped samples in terms of higher conductivity inside the TiO₂ NTs and enhancement of charge-transfer processes.

Therefore, photocurrent densities increased with increasing Re due to the higher active area of the NTs in contact with the electrolyte, whereas the increase in photocurrent densities observed with H⁺-doping can be ascribed either to the passivation of surface trap states or to an increase in NTs conductivity. Furthermore, it is evident from **Figure 4** that there is a synergistic effect between the hydrodynamic conditions and the H⁺-doping, which arises from the higher active areas of the samples anodized at Re > 0, thus enhancing the intercalation of H⁺ into the TiO₂ NTs structure. The overall increase in photocurrent density, Δi_{ph} , for H⁺-doped TiO₂ NTs synthesized under hydrodynamic conditions with respect to the undoped TiO₂ NTs formed at Re = 0 may be expressed as follows:

$$\Delta i_{ph} = \Delta i_{ph|Re} + \Delta i_{ph|H^+} + \Delta i_{ph|syn} \quad (1)$$

where $\Delta i_{ph|Re}$ is the increase in photocurrent due to the increase in Re, $\Delta i_{ph|H^+}$ is the increase in photocurrent due to H⁺-doping and $\Delta i_{ph|syn}$ is the contribution arising from the synergistic effect of hydrodynamic conditions and H⁺-doping. $\Delta i_{ph|Re}$ and $\Delta i_{ph|H^+}$ in the present study are given by the increase in photocurrent density (measured at 0.55 V_{Ag/AgCl}, **Figure 4**) when increasing Re from a value of 0 to 600 (0.014 mA cm⁻²) and when doping the sample synthesised at Re = 0 with H⁺ (0.016 mA cm⁻²), respectively. Hence, taking into account that the overall increase in photocurrent density (i.e., the photocurrent density of the H⁺-doped sample at Re = 600 minus the photocurrent density at Re = 0 without doping) is 0.050 mA cm⁻², the synergistic effect of hydrodynamic conditions and doping can be quantified as 0.020 mA cm⁻². The contributions of $\Delta i_{ph|Re}$, $\Delta i_{ph|H^+}$ and $\Delta i_{ph|syn}$ to the overall increase in photocurrent density are, respectively, 28.6%, 32.4% and 39%. Although none of these three factors is clearly dominant, the contribution of synergism was higher than the contributions of Re and H⁺-doping, thus indicating its importance.

Figure 5 shows, as an example, the photostability of the samples anodized at Re = 0 and Re = 600 with and without H⁺-doping, in a 1M KOH solution for 1 hour holding the applied potential at 0.55 V_{Ag/AgCl} under AM1.5 illumination. It can be observed that photocurrent density values (i_{ph}) did not vary with time, indicating that all the samples were resistant against photocorrosion and that the H⁺-doping process was stable.

3.5. EIS measurements and Mott-Schottky analysis

In order to study the influence of hydrodynamic conditions during TiO₂ NTs formation and H⁺-doping on the electrochemical and electronic properties of the TiO₂ photoanode/electrolyte interfase, EIS measurements and MS analysis were conducted for the different samples. **Figure 6** shows the Nyquist (**Figure 6a**) and Bode-phase (**Figure 6b**) plots of the TiO₂ NTs synthesized at Re = 0 and Re = 600, with and without H⁺-doping. The electrical equivalent circuit used to simulate the EIS experimental data is also shown in **Figure 6c**.

The shape of Nyquist plots is characterized in this case by one or two distorted small semicircles at high and intermediate frequencies followed by an unfinished semicircle at low frequencies, with a much higher amplitude. From Bode-phase plots, the presence of three time constants can be discerned, especially in the undoped samples. Although the impedance spectra for the H⁺-doped electrodes only exhibits two peaks, one at high frequencies and the other at intermediate-low frequencies, it is assumed that the last peak is actually the superposition of the time constants observed at medium and low frequencies in the other cases.

Experimental EIS data can be represented with an electrical equivalent circuit made up of three RC time constants, as shown in **Figure 6c**. Constant phase elements (CPEs) have been used instead of pure capacitors to account for frequency dispersion and non-ideality. According to the obtained values and to the literature, R_S is the electrolyte

resistance, the R_1CPE_1 time constant has been related to the TiO₂ nanoporous structure [8, 40, 41], the R_2CPE_2 time constant has been associated with the rutile layer formed at the bottom of the NTs array. The presence of rutile in the TiO₂ NTs has been confirmed above by Raman spectra (**Figure 2**). According to the literature [42-45] upon annealing at temperatures higher than 500° C (samples were annealed at 650° C in the present study) in an oxygen ambient, the NTs walls transform into anatase phase, and a layer at the bottom of the NTs converts into rutile. Hence, after annealing, the phase-structure of the TiO₂ NTs can be depicted as an anatase nanotube array atop a rutile layer. Finally, the R_3CPE_3 time constant has been related to a compact TiO₂ layer beneath the anatase nanotube array and the rutile layer [8, 46, 47].

The values of the different resistances in the equivalent circuit of **Figure 6c** are shown in **Table 1**. The value of the electrolyte resistance, R_s , is approximately constant in all the cases. Concerning the influence of hydrodynamic conditions during anodization on the values of the internal resistance of the nanostructures, it can be observed that R_l decreases to some extent under hydrodynamic conditions (from Re = 0 to Re = 600). The resistance of the compact TiO₂ layer formed beneath the NTs array, R_3 , takes very high values, regardless of the Re. The resistance of the rutile layer formed underneath the anatase NTs, R_2 , takes intermediate values between R_l and R_3 , although they are closer to R_l than to R_3 . The previous results imply (1) that the nanoporous overlayer has a higher conductivity than the rutile and compact TiO₂ underlayers, and (2) that the rutile layer cannot be regarded as a compact TiO₂ layer but as a transition layer between a compact layer and a porous one, whose conductivity is lower than that of the NTs but considerably higher than that of a TiO₂ compact film.

Regarding the influence of the H^+ -doping on the three resistances of the system, it can be observed from **Table 1** that R_1 decreases remarkably for the doped samples, especially for the sample anodized under hydrodynamic conditions ($Re = 600$). Values of R_2 and R_3 also decrease moderately with doping. These results indicate that the insertion of H^+ ions in the structure of TiO_2 enhances especially the conductivity of the anatase NTs, whereas the increase in the conductivity of the rutile and compact TiO_2 layers is not so important. The increase in conductivity of the NTs film when doping with H^+ could be explained, according to Boschloo et al. [39], by an increase in the density of donor-like impurities (interstitial hydrogen atoms). This statement will be verified through MS analysis.

Figure 7 shows the Mott-Schottky (M-S) plots at a frequency of 10 kHz for the undoped and H^+ -doped TiO_2 NTs formed at Re 0 and 600, in a 0.1M Na_2SO_4 solution at open circuit potential under dark conditions and at 25° C. These plots have been obtained at a frequency of 10 kHz since at this high value the capacitance dependence on frequency is eliminated [48-50]. As it can be observed in **Figure 7**, all the TiO_2 NTs show a positive slope as expected for n-type semiconductors.

The donor density, N_D , can be determined from the positive slopes of the straight lines in the M-S plots using the Mott-Schottky equation for an *n*-type semiconductor. Although the M-S equations were derived based on a flat electrode, this analysis has been widely used to irregular geometries with porous surfaces such as nanostructures [8, 24, 46, 47, 50-56]. Hence, a qualitative comparison between N_D values obtained for different TiO_2 layers and nanostructures is valid. The M-S expression for N_D is [49, 57, 58]:

$$N_D = \frac{2}{\varepsilon_0 e \sigma} \quad (2)$$

where ε is the dielectric constant of the TiO₂ layers (a value of 100 is assumed for the TiO₂ nanostructures [15, 55]), ε_0 is the vacuum permittivity ($8.85 \cdot 10^{-14}$ F/cm), e is the electron charge ($1.60 \cdot 10^{-19}$ C) and σ is the positive slope of each straight line in the M-S plots.

The N_D values have been calculated using the geometric area of the electrodes. It is remarkable that the H⁺-doped NTs present substantially lower slopes of the M-S plot compared to the undoped NTs, indicating an increase of the donor density for the doped samples. In fact N_D of the undoped NTs are 4.8 and 6.1×10^{16} cm⁻³ for Re = 0 and 600, respectively, while the values for the H⁺-doped NTs are considerably higher, 1.8 and 4.7×10^{17} cm⁻³. Since there is no change in the nanotube morphology after H⁺ intercalation, the increase in the donor density could be associated to an increase in the defects present in the TiO₂ NTs. Indeed, interstitial hydrogen atoms act as a donor impurity in TiO₂ [39]. The increase in the number of defects improves the charge transport along the NTs [8, 53, 54], as observed in EIS experiments, and shifts the Fermi level towards the conduction band, enhancing the charge separation at the semiconductor/electrolyte interface [24]. On the other hand, both for the undoped and H⁺-doped NTs, the hydrodynamic conditions during anodization increase the number of defects, this increase being much more noticeable in the doped NTs. This is in agreement with the photocurrent obtained for those samples (see **Figure 4**); i.e. the increase in the N_D improves the photocatalytic properties of the NTs, especially for the H⁺-doped-TiO₂ NTs at Re = 600. Therefore, there is a better charge transfer and transport in the doped-

NTs. Additionally, as explained above, it is believed that H^+ intercalation could passivate trap states originated in TiO_2 (for instance, Ti^{+4} and Ti^{+3}) which facilitates recombination [25, 33, 34, 38].

On the other hand, from the M-S plots it is possible to calculate the values of the flat band potential, as the intercept of the straight line with the potential axis. The flat band potential, that is the potential that needs to be applied to the semiconductor to reduce the band bending to zero, is related with the recombination probability of the semiconductor. In this way, the higher and more negative is the flat band potential value, the stronger the electrical field within the depleted space charge layer, which is the driving force to separate the photogenerated electron-hole pairs [48, 54]. **In Figure 7**, it can be observed that the flat band potentials of the doped NTs are shift to more negative values (-0.99 and $-0.81 V_{Ag/AgCl}$ for NTs anodized at $Re = 0$ and $Re = 600$, respectively), compared to the undoped NTs (-0.90 and $-0.76 V_{Ag/AgCl}$ for NTs anodized at $Re = 0$ and $Re = 600$, respectively). Therefore, in the doped NTs there is a displacement of the Fermi level towards the conduction band edge and leading to a larger band bending and electrical field within the depleted space charge layer [8, 24, 54]. Consequently, the recombination probability is lower for these samples. The flat band potential values for the NTs obtained under static conditions, are slightly more negative than the values calculated for the NTs anodized at $Re = 600$. This indicates that the recombination probability is lower for the TiO_2 NTs obtained at $Re = 0$. However, the higher photocurrents obtained in the photoelectrochemical water splitting for the NTs anodized under flowing conditions (**Figure 4**) are associated, among other factors, with the higher values of N_D obtained for these NTs, which clearly increases their photocatalytic performance.

4. CONCLUSIONS

Undoped and H⁺-doped TiO₂ NTs were formed in ethylene-glycol based electrolytes under different Re (from 0 to 600). Raman Confocal microscopy revealed that anatase and rutile crystalline phases were present after annealing the NTs at 650 °C for 1 h.

The use of hydrodynamic conditions during anodization led to an increase in the diameter of the pores present in the porous initiation layer together with an etched effect in the initiation layer that make the entrances of the NTs more accessible. On the other hand, flowing conditions allowed an accelerated growth of TiO₂ nanotube layers.

Higher photocurrent densities were obtained for samples anodized under hydrodynamic conditions, which is are directly related to an increase in the active area of the NTs exposed to the electrolyte with increasing Re. On the other hand, the blocking or passivation of surface recombination sites can explain the photocurrent enhancement of the H⁺-doped samples upon illumination.

A synergistic effect between the hydrodynamic conditions and the H⁺-doping was found to arise from the higher active areas of the samples anodized at Re > 0, thus enhancing the intercalation of H⁺ into the TiO₂ NTs structure. The contribution of synergism to the overall increase in photocurrent density (39%) was higher than the contributions of Re and H⁺-doping (28.6% and 32.4%, respectively).

The internal resistance of the nanostructures decreased to some extent under hydrodynamic conditions. It also decreased significantly upon H⁺-doping, especially at Re = 600, indicating that the insertion of H⁺ ions in the structure of TiO₂ enhanced the conductivity of the NTs.

The value of the donor density increased in the H⁺-doped NTs, which improved the charge transport along the NTs enhancing the charge separation at the semiconductor/electrolyte interface. On the other hand, both for the undoped and H⁺-doped NTs, the hydrodynamic conditions during anodization increased the number of defects, this increase being much more noticeable in the doped NTs, since H⁺ could passivate trap states originated in TiO₂. This is in agreement with the more negative flat band potential values obtained for the H⁺-doped NTs.

Acknowledgements: Authors would like to express their gratitude for the financial support to the Ministerio of Economía y Competitividad (Project CTQ2013-42494-R).

REFERENCES

- [1] J. M. Macak, H. Tsuchiya, A. Ghicov, K. Yasuda, R. Hahn, S. Bauer, P. Schmuki. TiO₂ nanotubes: Self-organized electrochemical formation, properties and applications, *Curr. Opin. Solid St. Mater. Sci.* 11 (2007) 3-18.
- [2] S. K. Mohapatra, M. Misra, V. K. Mahajan, K. S. Raja. A novel method for the synthesis of titania nanotubes using sonoelectrochemical method and its application for photoelectrochemical splitting of water, *J. Catal.* 246 (2007) 362-369.
- [3] G. Zhang, H. Huang, Y. Zhang, H. L. W. Chan, L. Zhou. Highly ordered nanoporous TiO₂ and its photocatalytic properties, *Electrochem. Commun.* 9 (2007) 2854-2858.
- [4] K. Shankar, G. K. Mor, H. E. Prakasam, S. Yoriya, M. Paulose, O. Varghese, C. A. Grimes. Highly-ordered TiO₂ nanotube arrays up to 220 μm in length: use in water photoelectrolysis and dye-sensitized solar cells, *Nanotechnology* 18 (2007) 065707 (11pp).
- [5] Z. Liu, B. Pesic, K. S. Raja, R. R. Rangaraju, M. Misra. Hydrogen generation under sunlight by self ordered TiO₂ nanotube arrays, *Int. J. Hydrogen Energ.* 34 (2009) 3250-3257.
- [6] Y. Y. Song, R. Lynch, D. Kim, P. Roy, P. Schmuki. TiO₂ Nanotubes: Efficient Suppression of Top Etching during Anodic Growth. Key to Improved High Aspect Ratio Geometries, *J. Electrochem. Soc.* 12 (2009) C17-C20.
- [7] D. Wang, Y. Liu, B. Yu, F. Zhou, W. Liu. TiO₂ Nanotubes with Tunable Morphology, Diameter, and Length: Synthesis and Photo-Electrical/Catalytic Performance, *Chem. Mater.* 21 (2009) 1198-1206.
- [8] S. Palmas, A. M. Polcaro, J. R. Ruiz, A. Da Pozzo, M. Mascia, A. Vacca. TiO₂ photoanodes for electrically enhanced water splitting, *Int. J. Hydrogen Energ.* 35 (2010) 6561-6570.
- [9] P. Roy, D. Kim, K. Lee, E. Spiecker, P. Schmuki. TiO₂ nanotubes and their application in dye-sensitized solar cells, *Nanoscale* 2 (2010) 45-59.
- [10] P. Roy, S. Berger, P. Schmuki. TiO₂ Nanotubes: Synthesis and Applications, *Angew. Chem. Int. Ed.* 50 (2011) 2904-2939.
- [11] S. J. Yoon, M. Lee, E. K. Kim, W. Lee, Y. C. Nah, N. K. Shrestha, S. H. Lee, S. H. Han. Influence of structural deformation on dye-sensitized solar cells with anodically fabricated self-organized TiO₂ nanotubes, *New J. Chem.* 35 (2011) 2521-2526.
- [12] R. Sánchez-Tovar, I. Paramasivam, K. Lee, P. Schmuki. Influence of hydrodynamic conditions on growth and geometry of anodic TiO₂ nanotubes and their use towards optimized DSSCs, *J. Mater. Chem.* 22 (2012) 12792-12795.

- [13] A. Mazzarolo, K. Lee, A. Vincenzo, P. Schmuki. Anodic TiO₂ nanotubes: Influence of top morphology on their photocatalytic performance, *Electrochem. Commun.* 22 (2012) 162-165.
- [14] D. Kim, A. Ghicov, P. Schmuki. TiO₂ Nanotube arrays: Elimination of disordered top layers ("nanograss") for improved photoconversion efficiency in dye-sensitized solar cells, *Electrochem. Commun.* 10 (2008) 1835-1838.
- [15] L.-K. Tsui, T. Homma, G. Zangari. Photocurrent Conversion in Anodized TiO₂ Nanotube Arrays: Effect of the Water Content in Anodizing Solutions, *J. Phys. Chem. C* 117 (2013) 6979-6989.
- [16] T. T. Isimjan, S. Rohani, A. K. Ray. Photoelectrochemical water splitting for hydrogen generation on highly ordered TiO₂ nanotubes fabricated by using Ti as cathode, *Int. J. Hydrogen Energ.* 37 (2012) 103-108.
- [17] H. E. Prakasam, K. Shankar, M. Paulose, O. K. Varghese, C. A. Grimes. A New Benchmark for TiO₂ Nanotube Array Growth by Anodization, *J. Phys. Chem. C* 111 (2007) 7235-7241.
- [18] D. Regonini, C. R. Bowen, A. Jaroenworuluck, R. Stevens. A review of growth mechanism, structure and crystallinity of anodized TiO₂ nanotubes, *Mater. Sci. Eng. R* 74 (2013) 377-406.
- [19] Y. Li, H. Yu, W. Song, G. Li, B. Yi, Z. Shao. A novel photoelectrochemical cell with self-organized TiO₂ nanotubes as photoanodes for hydrogen generation, *Int. J. Hydrogen Energ.* 36 (2011) 14374-14380.
- [20] Q. Gui, D. Yu, D. Li, Y. Song, X. Zhu, L. Cao, S. Zhang, W. Ma, S. You. Efficient suppression of nanograss during porous anodic TiO₂ nanotubes growth, *Appl. Surf. Sci.* 314 (2014) 505-509.
- [21] J. Yang, X. Wang, X. Yang, J. Li, X. Zhang, J. Zhao. Energy storage ability and anti-corrosion properties of Bi-doped TiO₂ nanotube arrays, *Electrochim. Acta* 169 (2015) 227-232.
- [22] M. M. Momeni, Y. Ghayeb, Z. Ghonchehi. Fabrication and characterization of copper doped TiO₂ nanotube arrays by in situ electrochemical method as efficient visible-light photocatalyst, *Ceram. Int.* 41 (2015) 8735-8741.
- [23] S. Sreekantan, R. Hazan, Z. Lockman. Photoactivity of anatase-rutile TiO₂ nanotubes formed by anodization method, *Thin Solid Films* 518 (2009) 16-21.
- [24] G. Wang, H. Wang, Y. Ling, Y. Tang, X. Yang, R. C. Fitzmorris, C. Wang, J. Z. Zhang, Y. Li. Hydrogen-Treated TiO₂ Nanowire Arrays for Photoelectrochemical Water Splitting, *Nano Lett.* 11 (2011) 3026-3033.
- [25] B. H. Meekins, P. V. Kamat. Got TiO₂ Nanotubes? Lithium Ion Intercalation Can Boost Their Photoelectrochemical Performance, *ACS Nano* 3 (2009) 3437-3446.

- [26] J. Wang, L. Zhao, V. S. Y. Lin, Z. Lin. Formation of various TiO₂ nanostructures from electrochemically anodized titanium, *J. Mater. Chem.* 19 (2009) 3682-3687.
- [27] H. Lu, J. Zhao, L. Li, L. Gong, J. Zheng, L. Zhang, Z. Wang, J. Zhang, Z. Zhu. Selective oxidation of sacrificial ethanol over TiO₂-based photocatalysts during water splitting, *Energy Environ. Sci.* 4 (2011) 3384-3388.
- [28] F. D. Hardcastle. Raman Spectroscopy of Titania (TiO₂) Nanotubular Water-Splitting Catalysts, *J. Arkansas Acad. Sci.* 65 (2011) 43-48.
- [29] D. Regonini, A. Jaroenworuluck, R. Stevens, C. R. Bowen. Effect of heat treatment on the properties and structure of TiO₂ nanotubes: phase composition and chemical composition, *Surf. Interface Anal.* 42 (2010) 139-144.
- [30] W. F. Zhang, Y. L. He, M. S. Zhang, Z. Yin, Q. Chen. Raman scattering study on anatase TiO₂ nanocrystals, *J. Phys. D: Appl. Phys.* 33 (2000) 912.
- [31] R. Sánchez-Tovar, K. Lee, J. García-Antón, P. Schmuki. Formation of anodic TiO₂ nanotube or nanosponge morphology determined by the electrolyte hydrodynamic conditions, *Electrochem. Commun.* 26 (2013) 1-4.
- [32] J. M. Macak, H. Hildebrand, U. Marten-Jahns, P. Schmuki. Mechanistic aspects and growth of large diameter self-organized TiO₂ nanotubes, *J. Electroanal. Chem.* 621 (2008) 254-266.
- [33] L. k. Tsui, M. Saito, T. Homma, G. Zangari. Trap-state passivation of titania nanotubes by electrochemical doping for enhanced photoelectrochemical performance, *J. Mater. Chem. A* 3 (2015) 360-367.
- [34] R. van de Krol, A. Goossens, J. Schoonman. Spatial Extent of Lithium Intercalation in Anatase TiO₂, *J. Phys. Chem. B* 103 (1999) 7151-7159.
- [35] T. Berger, M. Sterrer, O. Diwald, E. Knözinger, D. Panayotov, T. L. Thompson, J. T. Yates. Light-Induced Charge Separation in Anatase TiO₂ Particles, *J. Phys. Chem. B* 109 (2005) 6061-6068.
- [36] Sh. C. Ke, T. C. Wang, M. S. Wong, N. O. Gopal. Low Temperature Kinetics and Energetics of the Electron and Hole Traps in Irradiated TiO₂ Nanoparticles as Revealed by EPR Spectroscopy, *J. Phys. Chem. B* 110 (2006) 11628-11634.
- [37] B. J. Morgan, G. W. Watson. Polaronic trapping of electrons and holes by native defects in anatase TiO₂, *Phys. Rev. B* 80 (2009) 233102.
- [38] U. Kang, H. Park. Lithium ion-inserted TiO₂ nanotube array photoelectrocatalysts, *Appl. Catal. B-Environ.* 140-141 (2013) 233-240.
- [39] G. K. Boschloo, A. Goossens, J. Schoonman. Photoelectrochemical Study of Thin Anatase TiO₂ Films Prepared by Metallorganic Chemical Vapor Deposition, *J. Electrochem. Soc.* 144 (1997) 1311-1317.

- [40] P. Xiao, D. Liu, B. Batalla Garcia, S. Sepehri, Y. Zhang, G. Cao. Electrochemical and photoelectrical properties of titania nanotube arrays annealed in different gases, *Sensor Actuat. B-Chem.* 134 (2008) 367-372.
- [41] W. H. Leng, Z. Zhang, J. Q. Zhang, C. N. Cao. Investigation of the Kinetics of a TiO₂ Photoelectrocatalytic Reaction Involving Charge Transfer and Recombination through Surface States by Electrochemical Impedance Spectroscopy, *J. Phys. Chem. B* 109 (2005) 15008-15023.
- [42] G. K. Mor, O. K. Varghese, M. Paulose, C. A. Grimes. Transparent Highly Ordered TiO₂ Nanotube Arrays via Anodization of Titanium Thin Films, *Adv. Funct. Mater.* 15 (2005) 1291-1296.
- [43] G. K. Mor, O. K. Varghese, M. Paulose, K. Shankar, C. A. Grimes. A review on highly ordered, vertically oriented TiO₂ nanotube arrays: Fabrication, material properties, and solar energy applications, *Sol. Energy Mater. Sol. Cells* 90 (2006) 2011-2075.
- [44] Y. Yang, X. Wang, L. Li. Crystallization and Phase Transition of Titanium Oxide Nanotube Arrays, *J. Am. Ceram. Soc.* 91 (2008) 632-635.
- [45] X. Liu, J. Lin, Y. H. Tsang, X. Chen, P. Hing, H. Huang. Improved anatase phase stability in small diameter TiO₂ nanotube arrays for high performance dye-sensitized solar cells, *J. Alloys Compd.* 607 (2014) 50-53.
- [46] A. G. Muñoz, Q. Chen, P. Schmuki. Interfacial properties of self-organized TiO₂ nanotubes studied by impedance spectroscopy, *J. Solid State Electrochem.* 11 (2007) 1077-1084.
- [47] A. G. Muñoz. Semiconducting properties of self-organized TiO₂ nanotubes, *Electrochim. Acta* 52 (2007) 4167-4176.
- [48] M. Radecka, M. Rekas, A. Trenczek-Zajac, K. Zakrzewska. Importance of the band gap energy and flat band potential for application of modified TiO₂ photoanodes in water photolysis, *J. Power Sources* 181 (2008) 46-55.
- [49] R. M. Fernández-Domene, E. Blasco-Tamarit, D. M. García-García, J. García-Antón. Passivity Breakdown of Titanium in LiBr solutions, *J. Electrochem. Soc.* 161 (2014) C25-C35.
- [50] X. Lu, G. Wang, T. Zhai, M. Yu, J. Gan, Y. Tong, Y. Li. Hydrogenated TiO₂ Nanotube Arrays for Supercapacitors, *Nano Lett.* 12 (2012) 1690-1696.
- [51] S. Palmas, A. Da Pozzo, M. Mascia, A. Vacca, A. Ardu, R. Matarrese, I. Nova. Effect of the preparation conditions on the performance of TiO₂ nanotube arrays obtained by electrochemical oxidation, *Int. J. Hydrogen Energ.* 36 (2011) 8894-8901.

- [52] D. P. Oyarzún, R. Córdova, O. E. Linarez Pérez, E. Muñoz, R. Henríquez, M. López Teijelo, H. Gómez. Morphological, electrochemical and photoelectrochemical characterization of nanotubular TiO₂ synthesized electrochemically from different electrolytes, *J. Solid State Electrochem.* 15 (2011) 2265-2275.
- [53] L. Yu, Z. Wang, L. Shi, S. Yuan, Y. Zhao, J. Fang, W. Deng. Photoelectrocatalytic performance of TiO₂ nanoparticles incorporated TiO₂ nanotube arrays, *Appl. Catal. B-Environ.* 113-114 (2012) 318-325.
- [54] D. Wang, X. Zhang, P. Sun, S. Lu, L. Wang, C. Wang, Y. Liu. Photoelectrochemical Water Splitting with Rutile TiO₂ Nanowires Array: Synergistic Effect of Hydrogen Treatment and Surface Modification with Anatase Nanoparticles, *Electrochim. Acta* 130 (2014) 290-295.
- [55] L. Ainouche, L. Hamadou, A. Kadri, N. Benbrahim, D. Bradai. Interfacial Barrier Layer Properties of Three Generations of TiO₂ Nanotube Arrays, *Electrochim. Acta* 133 (2014) 597-609.
- [56] R. Sánchez-Tovar, R. M. Fernández-Domene, D. M. García-García, J. García-Antón. Enhancement of photoelectrochemical activity for water splitting by controlling hydrodynamic conditions on titanium anodization, *J. Power Sources* 286 (2015) 224-231.
- [57] Z. Jiang, X. Dai, H. Middleton. Investigation on passivity of titanium under steady-state conditions in acidic solutions, *Mater. Chem. Phys.* 126 (2011) 859-865.
- [58] A. M. Schmidt, D. S. Azambuja, E. M. A. Martini. Semiconductive properties of titanium anodic oxide films in McIlvaine buffer solution, *Corros. Sci.* 48 (2006) 2901-2912.

Tables captions

Table 1. Resistance values for the different samples anodized under static ($Re = 0$) and hydrodynamic ($Re = 600$) conditions, as well as for the H^+ -doped samples anodized at $Re = 0$ and $Re = 600$.

Figures captions

Figure 1. FE-SEM images of the top-view of the TiO_2 NTs anodized at 55 V, during 30 min at $Re = 0$ (a) and $Re = 600$ (b and c, the inset in c shows the cross sectional view of the NTs). (d) NTs thickness vs Re .

Figure 2. Raman confocal laser spectra of the amorphous and annealed ($650\text{ }^\circ\text{C}$ -1 h) TiO_2 NTs anodized at 55 V, during 30 min at $Re = 600$.

Figure 3. Current density transients obtained during the potentiostatic anodization of Ti at 55 V at different Re .

Figure 4. Photovoltammograms for (a) TiO_2 NTs synthesized at different Re , and (b) TiO_2 NTs anodized at $Re = 0$ and $Re = 600$ and doped with H^+ .

Figure 5. Photostability of the samples anodised at $Re = 0$ and $Re = 600$ with and without H^+ -doping.

Figure 6. Experimental Nyquist (a) and Bode-phase (b) plots for the samples anodized at $Re = 0$ and $Re = 600$, with and without H^+ -doping; (c) electrical equivalent circuit used to simulate experimental EIS data.

Figure 7. Mott Schottky plots of the undoped and doped nanotubes anodized at 55 V, during 30 min at $Re = 0$ and $Re = 600$, respectively.

Table 1

<i>Re</i>	$R_s/\Omega \text{ cm}^2$	$R_l/k\Omega \text{ cm}^2$	$R_2/k\Omega \text{ cm}^2$	$R_3/k\Omega \text{ cm}^2$	$\chi^2 (\times 10^{-3})$
0	45 ± 4	6.6 ± 1.5	86 ± 21	1936 ± 488	0.3
600	41 ± 8	4.1 ± 2.2	66 ± 22	2407 ± 637	1.3
0 D	33 ± 7	1.0 ± 0.3	64 ± 18	1071 ± 222	0.7
600 D	37 ± 6	0.3 ± 0.1	38 ± 14	1430 ± 243	0.8

Figure 1

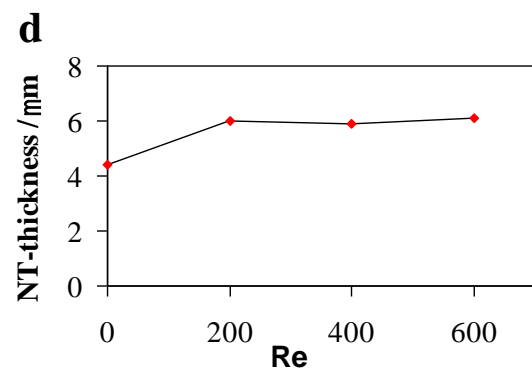
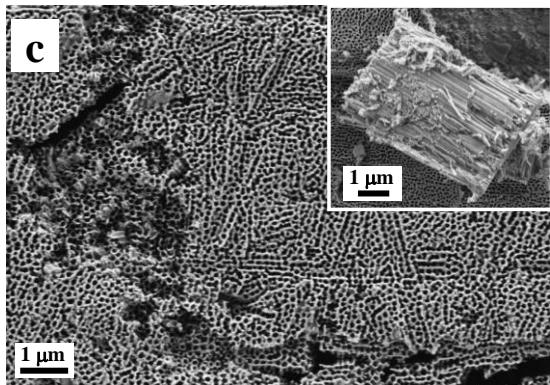
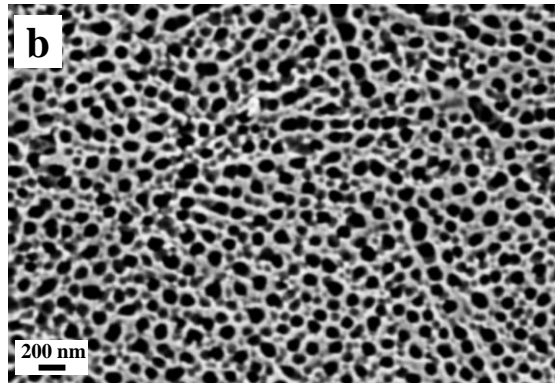
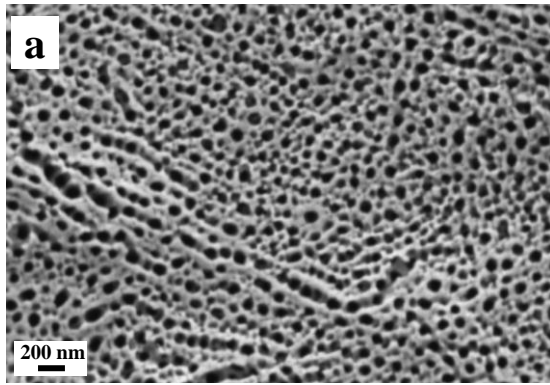


Figure 2

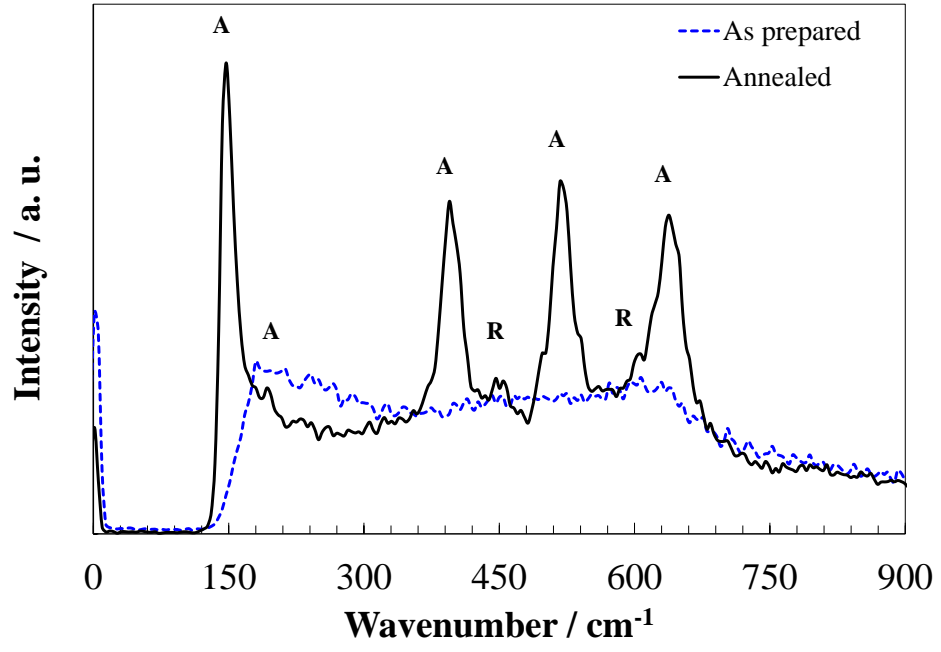


Figure 3

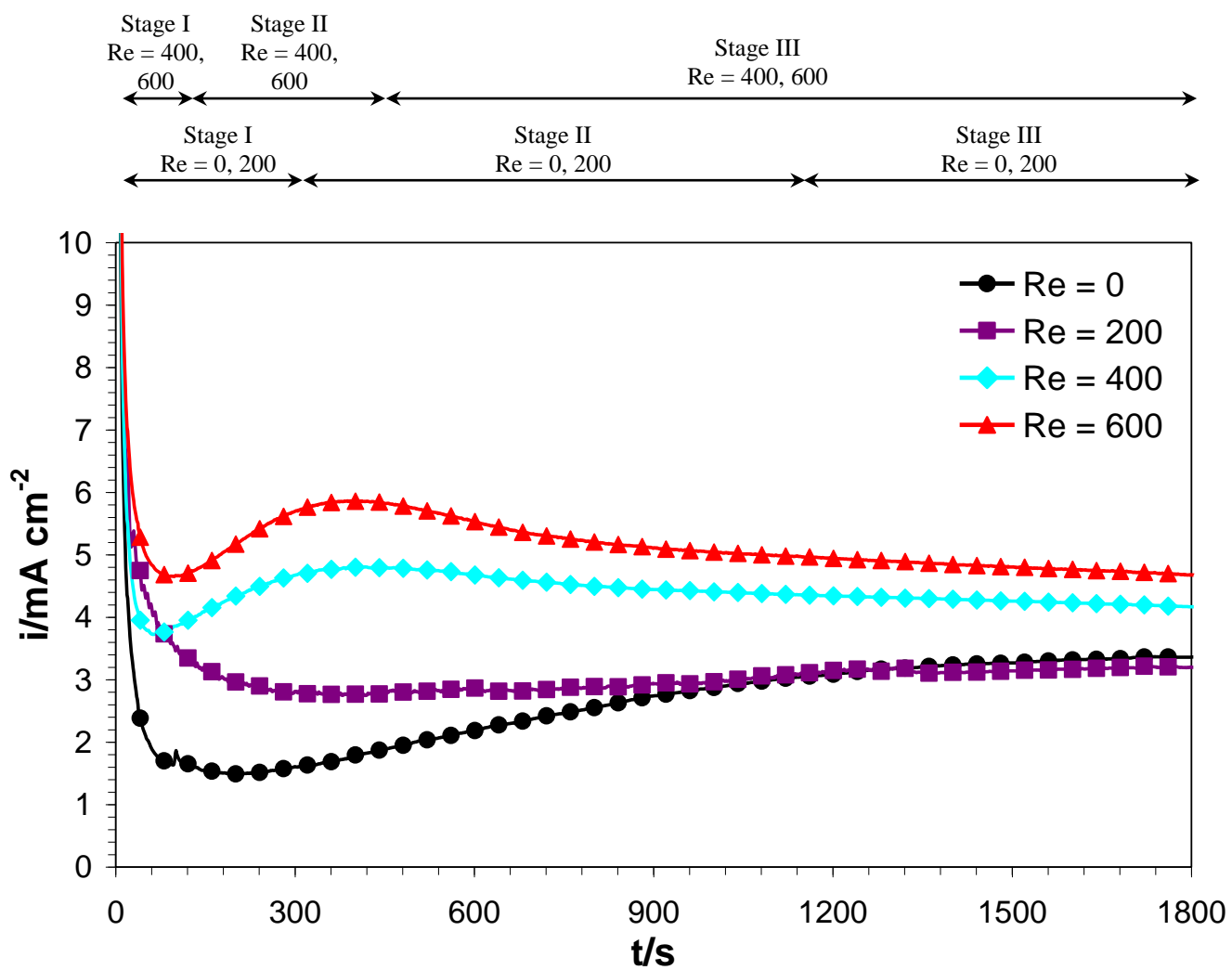


Figure 4

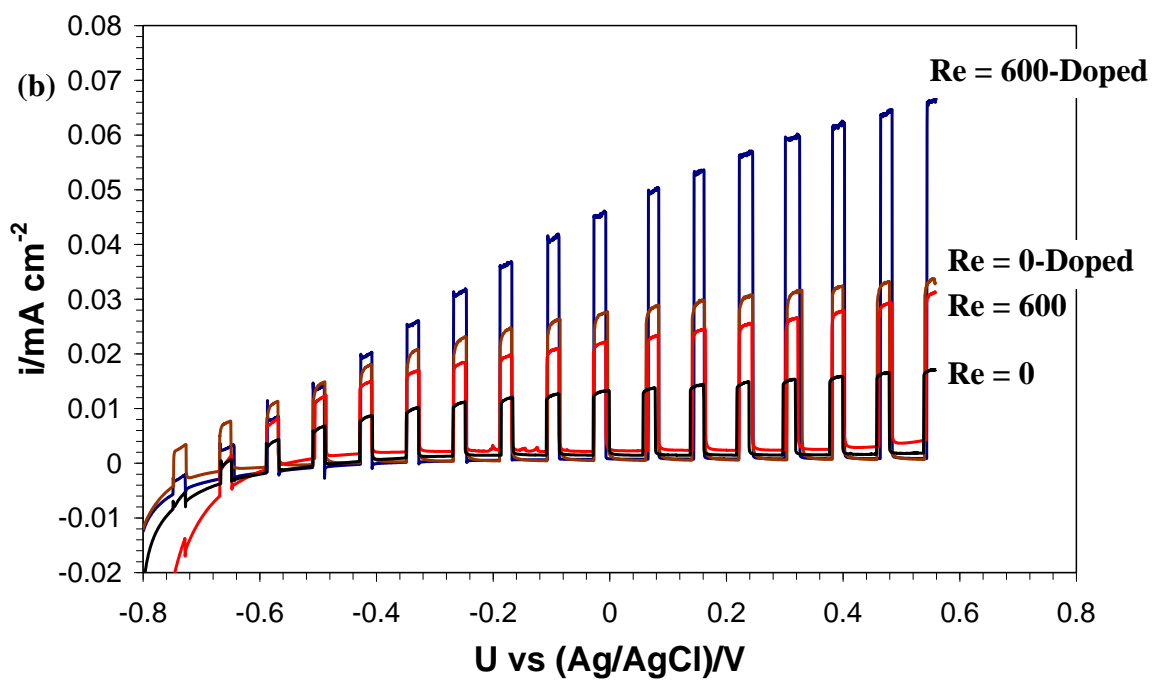
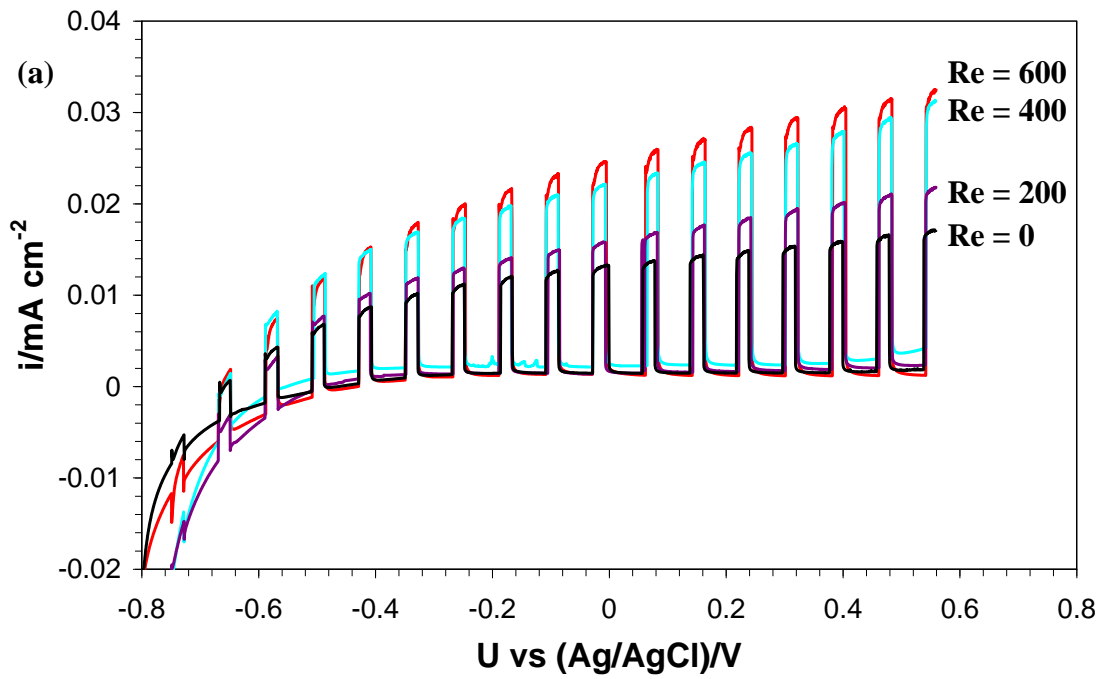


Figure 5

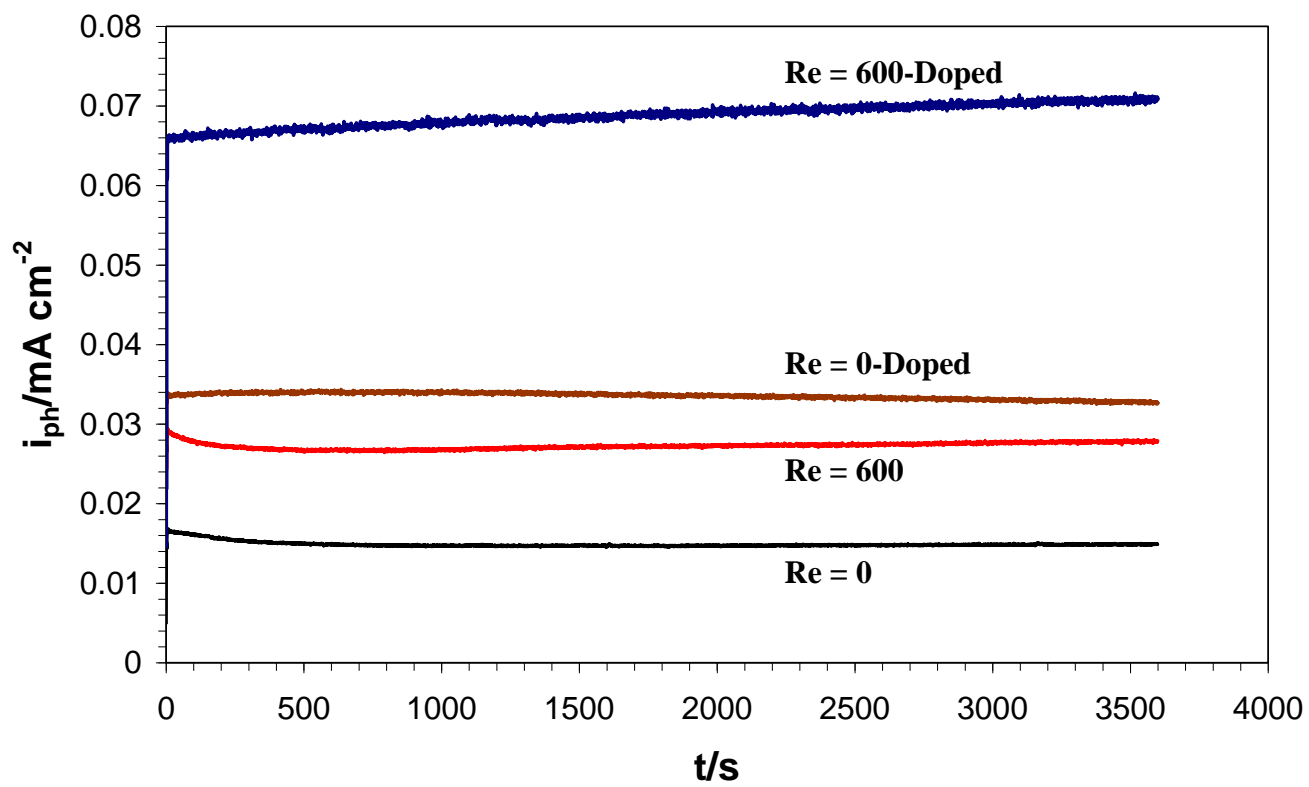


Figure 6

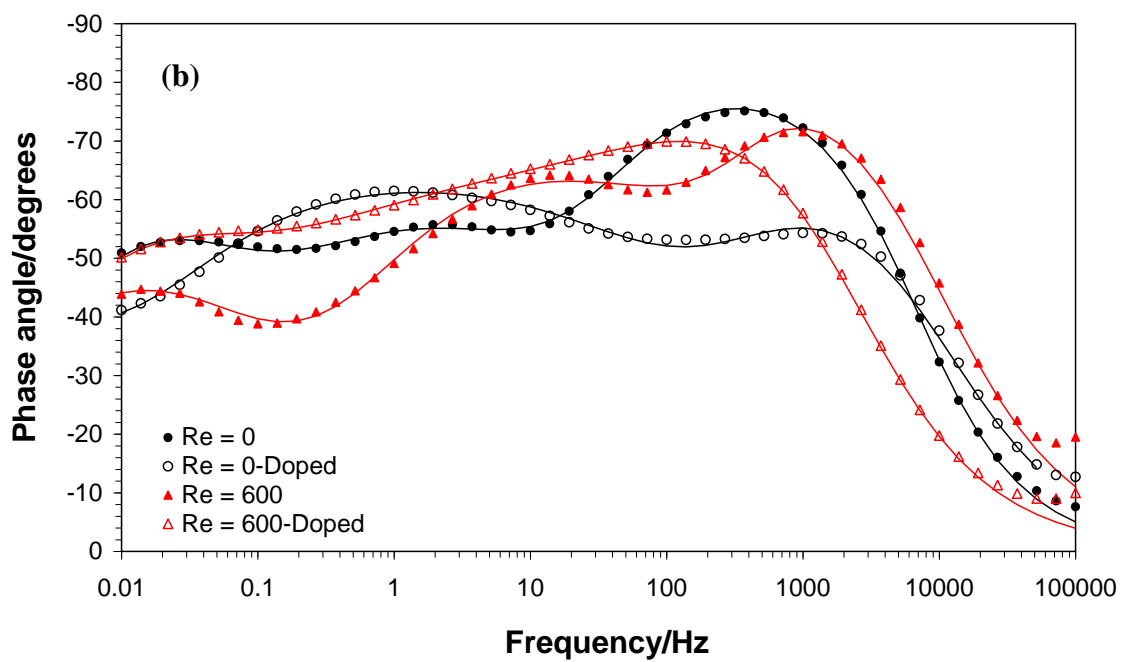
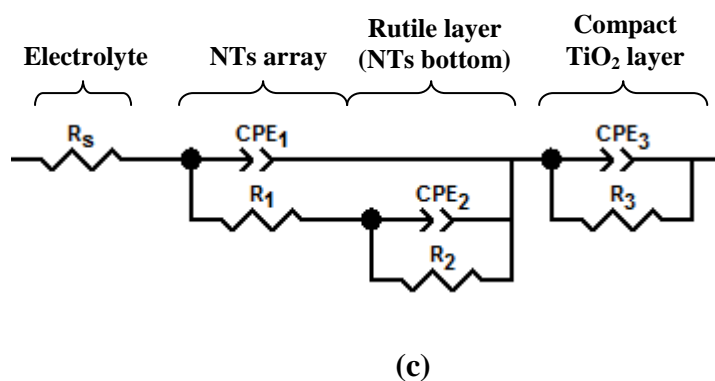
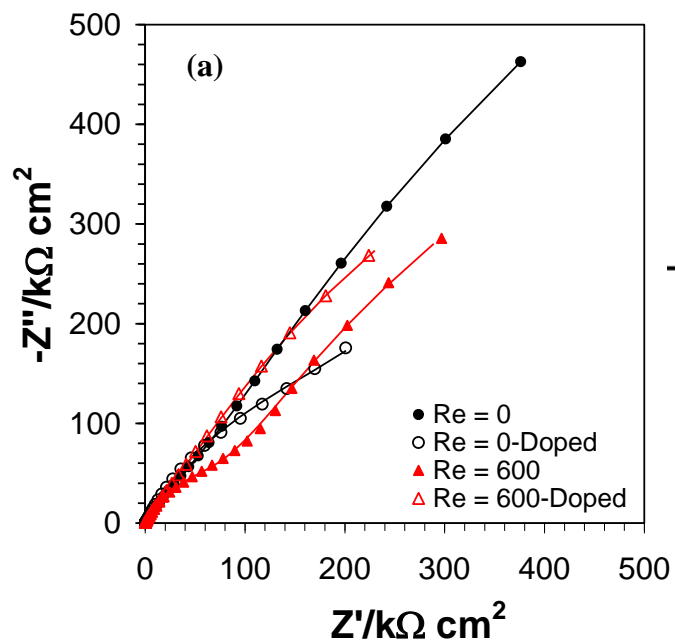


Figure 7

